analytical chemistry

Article

Cite This: Anal. Chem. 2019, 91, 9792−9799

pubs.acs.org/ac

Electric Triggering for Enhanced Control of Droplet Generation

Daihyun Kim,[†,‡] Austin Echelmeier,[†,‡] Jorvani Cruz Villarreal,[†,‡] Sahir Gandhi,[†,‡] Sebastian Quintana,[†,‡] Ana Egatz-Gomez,[†,‡] and Alexandra Ros*[,†,‡]

[†]School of Molecular Sciences, Arizona State University, Tempe, Arizona 85287, United States

[‡]Center for Applied Structural Discovery, The Biodesign Institute, Arizona State University, Tempe, Arizona 85281, United States

Supporting Information

ABSTRACT: Serial femtosecond crystallography (SFX) is a powerful technique that uses X-ray free-electron lasers (XFEL) to determine structures of biomolecular complexes. Specifically, it benefits the study of atomic resolution structures of large membrane protein complexes and time-resolved reactions with crystallography. One major drawback of SFX studies with XFELs is the consumption of large amounts of a protein crystal sample to collect a complete X-ray diffraction data set for high-resolution crystal structures. This increases the time and resources required for sample preparation and experimentation. The intrinsic pulsed nature of all current X-ray sources is a major reason why such large amounts of sample are required. Any crystal sample that is delivered in the path of the X-ray beam during its "off-time" is wasted. To address this large sample consumption issue, we developed a 3D printed microfluidic system with integrated metal electrodes for water-in-oil droplet generation to dynamically create and manipulate aqueous droplets. We demonstrate on-demand droplet generation using DC potentials and the ability to tune the frequency of droplet generation through the application of AC potentials. More importantly, to assist with the synchronization of droplets and XFEL pulses, we show that the device can induce a phase shift in the base droplet generation frequency. This novel approach to droplet generation has the potential to reduce sample waste by more than 95% for SFX experiments with XFELs performed with liquid jets and can operate under low- and high-pressure liquid injection systems.

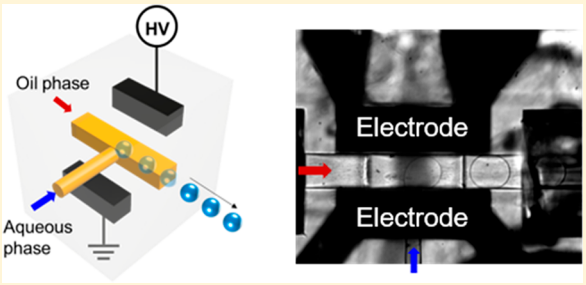

Serial femtosecond crystallography (SFX) is an emerging crystallography technique and among the most powerful tools to determine structures of proteins. SFX allows for an atomic level analysis of challenging protein structures, time-resolved diffraction at room temperature, and the study of submicrometer- and micrometer-sized protein crystals, which are considered too small for conventional crystallography.[1−5] In most cases, SFX is performed by employing a high-intensity femtosecond X-ray free-electron laser (XFEL). The XFEL pulses irradiate ideally one protein crystal at a time, and the resulting diffraction pattern is acquired before the protein crystal is destroyed.[4−6] Since many thousands of such diffraction patterns are required to construct an electron density map of a protein structure, SFX experiments with XFELs commonly use a continuous sample delivery method, which is realized with a gas dynamic virtual nozzle (GDVN).[2,7] Using this delivery method, protein crystals are jetted into the path of a pulsed X-ray beam, either in a vacuum chamber[8] or under atmospheric pressure.[9] This continuous sample delivery method coupled with the intrinsic pulsed nature of XFELs is the primary reason why SFX experiments consume a large amount (up to grams) of protein sample. With the current XFEL repetition rates and the flow rates required for a stable liquid jet injection through a GDVN, nearly 95−99% of injected protein crystals are wasted in between laser pulses. This is particularly problematic for proteins that can only be produced in small quantities.[9] Any wastage of sample increases costs and experimentation time enormously.

To circumvent the problem of large sample loss due to the inherent pulsed nature of XFELs, several methods for sample delivery have been proposed including reduction of the speed of sample delivery, drop on-demand injection, interrupting the jet of a GDVN, or breaking the continuous sample delivery into droplets through a segmented flow approach.[10] Reduced sample speed approaches rely on slowing down the speed of the jet extruding the crystal slurries. Weierstall et al. developed a viscous lipidic cubic phase (LCP) injector that extrudes sample at low speeds with a reduction in sample waste by a factor of 20.[11] Other viscous media have been reported to be suitable for LCP injection, including poly(ethylene oxide)s, hydrogels, agarose, or grease, as recently summarized.[12] With agarose, for example, the sample waste could be reduced by up to 2 orders of magnitude.[9] However, the LCP injector approach is not suited for all SFX experiments because many protein crystals cannot be grown in or are unstable when mixed into LCP or other viscous media. In addition, large background X-ray scattering is induced because of the large

Received: March 21, 2019
Accepted: July 1, 2019
Published: July 1, 2019

DOI: 10.1021/acs.analchem.9b01449
Anal. Chem. 2019, 91, 9792−9799

diameter of the LCP jet.[8,11,13] Furthermore, to populate an undamaged crystal for each pulse, XFELs that operate at MHz X-ray pulse frequencies require a high velocity jet (>50 m/s).[14] One such example is the European XFEL (EuXFEL), which delivers pulse trains that repeat at 10 Hz, whereas each train may contain several hundred MHz frequency pulses.[15] The microfluidic electrokinetic sample holder (MESH) is another reduced sample consumption technique with continuous sample introduction at low flow rates,[16] whereas the concentric MESH (CoMESH) injector alleviates issues associated with a vacuum.[17]

An alternative approach consists of droplet injection. For example, Mafuné et al. developed a setup that introduced pulsed liquid droplets containing protein crystals in the path of X-rays[18] delivering sample *via* a piezoelectric element where the droplet release is stimulated by an external trigger.[19] This injector has been used at the SPring-8 Angstrom Compact free-electron LAser (SACLA) for SFX studies on lysozyme[19] and bacteriorhodopsin.[20] Other approaches employed acoustic droplet ejection (ADE). Roessler et al. have generated crystals-containing droplets on-demand and have demonstrated the intersection of the majority of generated droplets with the X-ray pulses.[21] This approach is, however, affected by crystal settling, generates fairly large droplets and introduces large background scattering. ADE has also been combined with a conveyer belt system for time-resolved crystallography where droplets are ejected acoustically onto the conveyor belt. This approach is also known as droplet on tape (DOT) and facilitates the time-resolved study of photoinitiated and gas-initiated reactions.[22,23] However, while sample delivery on tape has allowed time-resolved studies,[24] the delivery of droplets on a tape in combination with ADE is not suitable for time-resolved studies where substrates are in solution.

Segmented sample delivery for XFELs has been proposed on microfluidic platforms previously by Echelmeier et al.[25] based on established two phase droplet manipulation for droplet generation, transport, sorting, coalescence and splitting on microfluidic devices.[26−28] Conventionally, by introducing an immiscible fluid into another, droplets or a segmented flow can be produced passively for sample delivery.[29,30] We recently developed a method based on this segmented-flow approach to generate droplets carrying crystals and conserve sample at SFX experiments.[31] In order to conserve substantial sample amounts, the droplet generation and the X-ray pulses at the XFEL must not only be of identical frequency, but also in phase. It is also important to ensure that the frequency of the segmented droplet approach is compatible with current XFEL repetition frequencies ranging from 10 up to 120 Hz. Thus, precise control of the droplet generation frequency and phase is necessary, which can be established with an external stimuli such as electrical, magnetic, centrifugal, optical, thermal, or mechanical approaches.[29,30] Among these, electrical stimuli have been demonstrated to be useful for controlling droplet generation by tuning of electrowetting characteristics when a direct current (DC) or an alternating current (AC) potential is applied between sets of electrodes.[32−34]

In this paper, we present a 3D printed microfluidic device with integrated metal electrodes to dynamically create and manipulate aqueous droplets. This approach is designed to address the limitations of continuous flow protein crystal sample delivery methods in SFX experiments. Based on the type and duration of the electrical potential applied between a set of electrodes, we are able to generate droplets in various modes. These include (i) on-demand droplets where a droplet is generated upon application of an electrical pulse, (ii) inducing a phase shift in a stream of continuous droplets by the application of an external electrical trigger signal and (iii) tunable frequency modulation, where the frequency of a continuous stream of droplets is changed for the duration of the applied electrical pulse. These three modes may be suitable for the synchronization of the pulsed XFELs with sample delivery in picoliter to nanoliter droplets. We further relate the observed phenomena with physical interface phenomena allowing for the operation in the three triggering modes. The presented microfluidic device can be fully integrated into SFX injection systems and is expected to reduce protein sample consumption for SFX experiments significantly in the future.

EXPERIMENTAL SECTION

All materials and chemicals used as well as data acquisition details are described in the Supporting Information.

Preparation of 3D Printed Device. The droplet generator device was designed using Autodesk Fusion 360 (Autodesk, CA, U.S.A.) and 3D printed using a Photonic Professional GT Printer (Nanoscribe GmbH, Germany) as described previously.[31] In brief, IP-S photoresist was used to print *via* dip-in laser lithography and two-photon polymerization. The printed device was developed in SU-8 developer and washed with isopropyl alcohol. Polished fused-silica capillaries, 30 cm in length, were inserted in the fluidic channels of the droplet generator and glued permanently with epoxy. Both oil and aqueous channels were then coated with Novec 1720 as described in previous work.[35]

To insert electrodes, the liquid gallium was loaded into a 1 μL glass syringe and immediately injected into electrode channels of the 3D printed device through the inlets[36] while vacuum was applied to the electrode channel outlets with a vacuum pump (Model 2027, Welch, Prospect, IL, U.S.A.). Subsequently, 5 cm long Ni−Cr wires (diameter = 320 μm) were attached to each metal electrode channel and connected to an external power source. An epoxy adhesive was then applied to the metal channel inlets and outlets and cured at room temperature for 1 h. Schematic drawings of the device are presented in Figure 1.

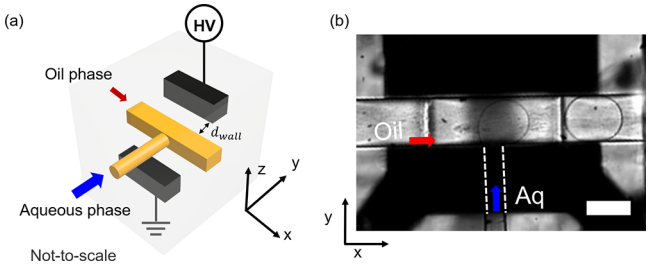

Figure 1. (a) 3D schematic representation of the droplet generator with fluidic T-junction (yellow) and two inlets for the aqueous phase and the oil phase. The diagonally arranged metal electrodes (black) were connected to an external power source (not-to-scale). The arrow shows the distance between the electrode and the fluidic channel along the *y*-axis. (b) A microscopic image shows a droplet generated at the T-junction. The flow directions of oil (red) and aqueous phase (blue) are depicted with arrows. The dashed lines indicate the portion of the aqueous channel masked by the solid electrodes. The scale bar represents 100 μm.

DOI: 10.1021/acs.analchem.9b01449
Anal. Chem. 2019, 91, 9792−9799

Fluidic Setup. A mixture of perfluorodecalin (PFD) and 1*H*,1*H*,2*H*,2*H*-perfluorooctanol (PFO) (v/v = 10/1) was used as the oil phase. Two mother liquor crystallization suspensions for proteins, termed buffer 1 and 2, were used as aqueous phase. Buffer 1 for crystallizing KDO8PS (3-deoxy-D-manno-octulosonate 8-phosphate synthase) contained 46 mM KCl, 8 mM tris hydrochloride (Tris-HCl), 7.2 w/v% 5K poly-(ethylene glycol)methyl ether (PEGME).[37] Buffer 2 for crystallizing photosystem I contained 5 mM 2-(nmorpholino)-ethanesulfonic acid (MES) at pH 6.4 and 0.02 v% of *n*-dodecyl *β*-D-maltoside (*β*-DDM).[9] The viscosity of oil and aqueous phase was measured with a viscometer (Brookfield LV DV-II+ Pro, U.S.A.) and resulted in 13.3 ± 0.5 cP and 3.6 ± 0.4 cP, respectively.

For experiments at low-pressure (<14 psi), a flow controller (MFCS-EZ, Fluigent, France) delivered liquid through aqueous and oil reservoirs of Fluiwells (Fluigent, France) to the device through 40 cm long fused-silica capillaries (100 μm inner diameter (ID) and 360 μm outer diameter (OD)). For high-pressure experiments (>14 psi), HPLC pumps (LC-20AD, Shimadzu Co., Japan) were connected to reservoirs filled with oil or aqueous phase as described previously to displace liquid toward the droplet generator.[31] Liquid-flow sensors SLI-0430 and SLG-0075 (Sensirion, Switzerland) monitored the flow rates after the reservoirs. PEEK tubings (250 μm ID and 1/16-in OD) with fittings and ferrules were used to connect the HPLC pumps to the reservoirs and sensors, while fused-silica capillaries and PicoClear unions were used downstream from the droplet generator. After any adjustment of the flow rates, the system was allowed to equilibrate for 5−10 min until pressures stabilized within the system. The aqueous flow rate (Q_a) range was between 0.2 and 5 μL/min, and the oil flow rate (Q_o) ranged between 5 and 25 μL/min.

RESULTS AND DISCUSSION

Delivering droplet suspensions at a defined frequency and synchronized with an XFEL laser will reduce the sample amount required for SFX experiments dramatically. Our approach to reduce the amount of sample wasted in SFX experiments consists of a microfluidic droplet generator fabricated using a high-resolution 3D printing technique. Droplet generation control is attained by applying a potential difference between embedded electrodes. Under pressure-driven flow, the shear forces induced by the oil phase acting on the aqueous phase elongate the aqueous droplets leaving the T-junction downstream, until eventually the droplets get pinched off.[30] The frequency of the resulting droplet generation is a complex interplay between the fluid viscosities, the surface tension of the involved interfaces, the channel geometry, as well as the flow rates and pressures acting in the system.

A representative schematic of the droplet generation device with integrated electrodes is shown in Figure 1a. Figure S1a depicts a computer-aided rendition of the device used for 3D printing and illustrates the T-junction, the microelectrodes, and their respective inlets and outlets for the melted metal in close proximity to the fluidic channels. The distance between the electrode and the fluidic channel along the *y*-axis is indicated as d_{wall} in Figure 1a. This distance was varied from 50 to 5 μm and could withstand experimental pressures ranging from a few up to several hundred psi and flow rates of 0.5−20 μL/min. Figure S1b shows the top view of an assembled droplet generator with inserted capillaries and integrated electrodes. A representative image of droplets generated at Q_o = 8 μL/min and Q_a = 1 μL/min is shown in Figure 1b.

Three different droplet generation modes based on DC or AC electric potentials were investigated, as shown in Figure 2.

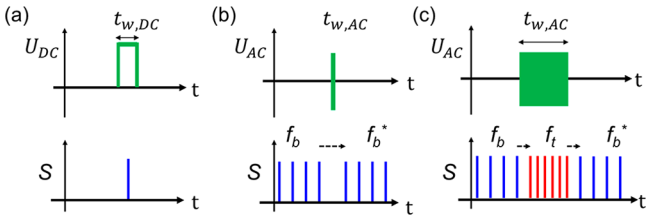

Figure 2. Overview of the three triggering modes. Applied DC or AC potentials with duration (t_w) and amplitude are shown in green in the top row. The corresponding droplet detector signal (S) is shown below each trace. The blue and red droplet detector signals correspond to the droplet generation frequency (prior (f_b) and after (f_{b*}) the trigger) and increased frequency (f_t), respectively. (a) In mode 1, on-demand droplet generation is induced by a DC pulse of amplitude U_{DC} for a duration $t_{w,DC}$. (b) In mode 2, a short pulse ($t_{w,AC}$ = 10 ms) of an AC potential with amplitude U_{AC} leads to a phase shift ($\Delta\phi$) in a continuous stream of generated droplets without affecting f_b. (c) In mode 3, a longer AC trigger signal ($t_{w,AC}$ > 100 ms) accelerates f_b (blue), into a faster droplet generation frequency f_t (red) for the duration of the applied signal.

The top row represents the applied trigger signal (green), and the bottom row represents the droplet signal obtained from the droplet detector (photodiode). In mode 1, no droplets are generated unless a potential is applied, serving as a "drop on-demand" method. Each DC electrical pulse generates a single droplet. Mode 1 generates droplets on-demand when a DC voltage with an amplitude, U_{DC} (210 V ≤ U_{DC} ≤ 1000 V) is applied for a duration, $t_{w,DC}$ (≥300 ms). In mode 2, an AC trigger potential with a peak amplitude (U_{AC}), a frequency (f_u), and a short duration ($t_{w,AC}$) is applied to induce a phase shift ($\Delta\phi$) in an already established droplet train with a stable frequency (f_b), as shown in Figure 2b. Characteristic for mode 2 is the recovery of f_{b*} after the application of the electrical trigger. Finally, mode 3 employs an AC electrical trigger signal with an amplitude U_{AC} (250 V ≤ U_{AC} < 400 V) and f_u (100 Hz ≤ f_u < 400 Hz) applied for $t_{w,AC}$ (>100 ms) as shown in Figure 2c. During the application of the electrical stimulus, f_b (blue) increases to a frequency f_t (red). After the electrical stimulus, the droplet generation frequency returns to f_{b*} (blue), which as in mode 2 is similar to f_b. The parameters we investigated for the operation of these three modes are summarized in Table S1 (see Supporting Information).

Mode 1: Drop On-Demand. The capability of a device to generate droplets on-demand is important as it allows a single aqueous droplet to be dispensed in the microfluidic chip with precise controllability over trigger timing. Thus, mode 1 can be used to synchronize the injection of protein crystal suspension droplets with XFEL pulses. To explore this mode, a low-pressure setup (<14 psi) with the PFD/PFO oil mixture as the oil phase and buffer 1 as the aqueous phase was employed. A DC potential in the 200 V ≤ U_{DC} ≤ 1000 V range with a duration of $t_{w,DC}$ = 300 ms was used as electrical stimulus. It was important to establish an equilibrium at the aqueous−oil interface in the microfluidic T-junction achieved by optimizing the pressures to both phases such that no droplets were generated while allowing the aqueous medium to protrude

DOI: 10.1021/acs.analchem.9b01449
Anal. Chem. 2019, 91, 9792−9799

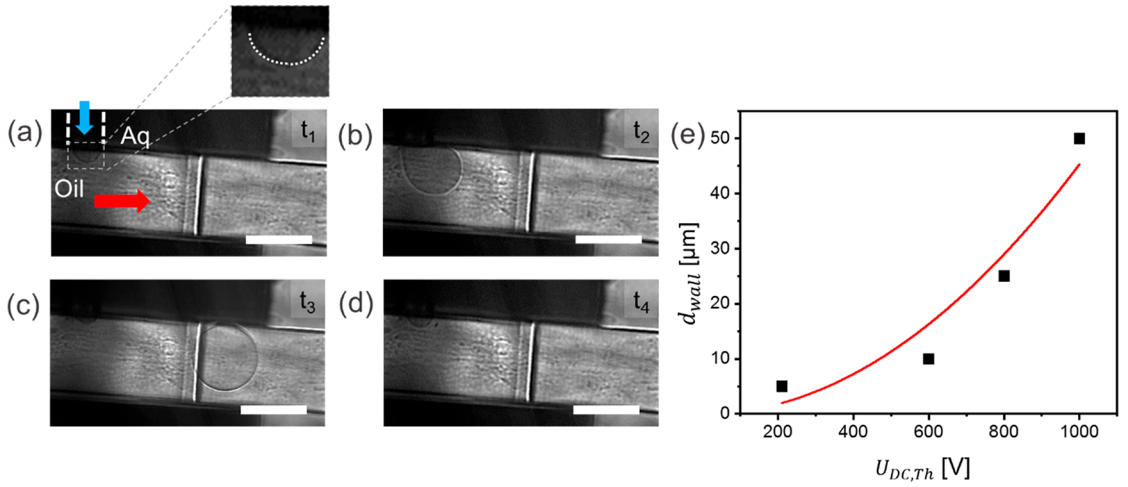

Figure 3. (a–d) Sequential droplet images at the T-junction in mode 1. (a) Snapshot of a stable interface (t = 0) between the oil (PFD:PFO 10/1, v/v) phase and aqueous phase (Buffer 1) at the T-junction; (b) A droplet composed of the aqueous phase medium is pulled out into the oil phase after a short DC pulse was applied (U_{DC} = 210 V, $t_{w,DC}$ = 300 ms); (c) The formed droplet leaving the T-junction, and (d) droplet generated is no longer in field of view. P_o was 197 mbar and P_a was 190 mbar. The flow in the fluidic channel proceeds from left to right. All scale bars represent 100 μm. (e) Relationship between d_{wall} and the threshold voltage for droplet generation. Origin software was used to create a quadratic trendline (red) for the relationship between d_{wall} and $U_{DC,Th}$.

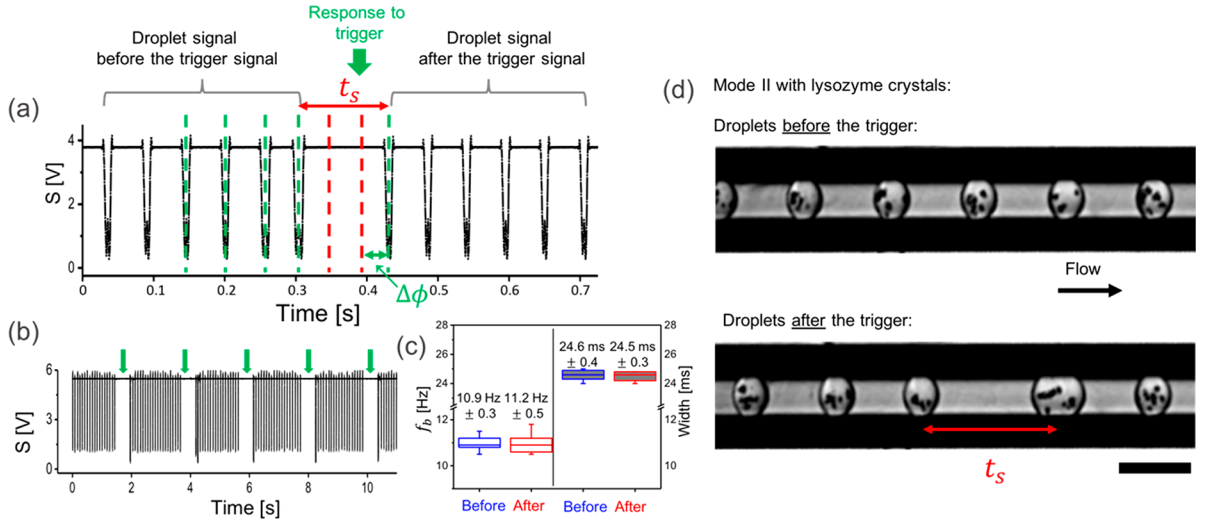

Figure 4. (a) A trace of stable droplet generation frequency (f_b) in mode 2. Upon application of an AC potential (U_{AC} = 250 V at f_u = 100 Hz, t_w = 10 ms), the droplet generation is shortly interrupted (response to trigger). This leads to a $\Delta\phi$, without change in f_b. The dashed red lines during t_s are representative of the droplets that would have been generated at f_b without a stimulus. (b) Example droplet trace showing multiple trigger signals (U_{AC} = 250 V at f_u = 100 Hz, $t_{w,AC}$ = 10 ms), all generating a similar response to the trigger (silent time), whereas the frequency f_{b*} recovers to f_b after each electrical trigger. The droplet signals were acquired using the droplet detector and recorded with Powerlab and Labchart (see Supporting Information for details). (c) Analysis of the droplet frequency and width over 10 s before and after the trigger. The base frequency and droplet length (in time) are consistent before and after the trigger with errors. In the box plots, boxes extend from the 25th to the 75th percentiles with a line at the median. Whiskers extend to the max/min data points. (d) Brightfield microscopy images of droplets containing lysozyme crystals before (top) and after (bottom) an electrical trigger signal (U_{AC} = 300 V at f_u = 100 Hz, $t_{w,AC}$ = 100 ms) in the outlet capillary. After the trigger, the t_S is indicated (red arrow) which leads to $\Delta\phi$ of 60 ms. Black spots within droplets are lysozyme crystals. The scale bar represents 200 μm.

slightly into the oil channel, as depicted in Figure 3a. Once this was achieved, DC trigger pulses of variable amplitudes but fixed $t_{w,DC}$ were tested until eventually a droplet was generated. This potential was characterized as the threshold potential, $U_{DC,Th}$. Below $U_{DC,Th}$, the aqueous–oil interface fluctuated, and no droplets were formed. Above $U_{DC,Th}$, one droplet was formed per stimulus pulse.

Figure 3a–d depicts typical sequential images recorded for on-demand droplet generation using a high-speed camera. Milliseconds after the trigger pulse started, a droplet was generated as observed in Figure 3 resulting in a volume of 240 ± 30 pL. A single droplet was successfully generated each time the stimulus was above $U_{DC,Th}$. Supporting Information Video S1 shows a series of single droplet on-demand generation events using a DC trigger signal ($U_{DC,Th}$ = 210 V and $t_{w,DC}$ = 300 ms) in the device (d_{wall} = 5 μm).

We further explored the relation between $U_{DC,Th}$ and d_{wall} (see Figure 3e). As d_{wall} was decreased from 50 to 5 μm, the required threshold potential, $U_{DC,Th}$, decreased from nearly 1000 to 210 V. When the applied potential was below the threshold, or the duration of the trigger was too short, $t_{w,DC}$ < 300 ms, the aqueous phase only fluctuated at the aqueous–oil

DOI: 10.1021/acs.analchem.9b01449
Anal. Chem. 2019, 91, 9792–9799

interface, and no droplet was released. Experiments showed that a DC pulse of at least 300 ms was required to induce droplets (data not shown). Each stimulus with a duration from 300 ms to 60 s resulted in a single droplet release. There was a minimum time interval required between two consecutive droplet generation events, which was observed to be around 300 ms. In conclusion, by controlling U_{DC} and $t_{w,DC}$, mode 1 can be used to trigger droplets on-demand in the device, with potential for synchronizing each droplet with an XFEL pulse. With our current experimental setup, the maximum frequency of on-demand droplet generation in this mode is about 1.7 Hz. While this droplet generation is below the typical XFEL repetition rates, improved design layouts and further studies will allow drop on-demand generation to reach a repetition frequency of at least 10 Hz. This would thus allow exploiting X-ray crystallography, taking advantage of the MHz bursts within the 10 Hz trains generated at the EuXFEL, since the droplet volumes cover the length of the MHz bursts.

Mode 2: Inducing a Phase Shift. The significance of mode 2 is underlined by the required synchronization of a droplet generation base frequency with the nontunable XFEL repetition rate. We thus explored the potential to synchronize the phase of the droplet generation frequency with the XFEL repetition rate, without changing the oil or aqueous flow rates by use of electrical stimulation in a device generating droplets at f_b and retard the droplet release for a defined time at the T-intersection to achieve a required $\Delta\phi$. This was explored *via* the application of a short AC trigger signal ($t_{w,AC}$ = 10 ms) to induce a delay in f_b. We chose to investigate mode 2 for the pulse train repetition frequency matching the EuXFEL of 10 Hz. A high-pressure setup as described in the methods section was used to mimic the XFEL facility requirements. A representative trace of the droplet frequency (f_b = 10.9 ± 0.3 Hz) is shown in Figure 4a, where Q_o = 6.5 and Q_a = 0.21 μL/min, generating droplets with an average volume of 378 ± 13 pL. While droplets were passively produced at the T-junction, a short AC trigger signal (U_{AC} = 250 V at f_u = 100 Hz, $t_{w,AC}$ = 10 ms) was applied, causing droplet generation to stop for a brief silent time (t_s = 54 ms), as shown in Figure 4a, after which droplet generation resumed at the base frequency (Figure 4c) within error margins. This can also be observed as a difference in the droplet distance resultant from the triggering event, as shown in Supplementary Video S2. The phase shift can thus be characterized by the following equation:

$$\Delta\phi = t_s - n\frac{1}{f_b} \tag{1}$$

where n represents the number of droplets that would be generated during t_s at f_b without the stimulus. The stimulus can be repeated as needed, as shown for a total of five consecutive stimuli (U_{AC} = 250 V at f_u = 100 Hz with $t_{w,AC}$ = 10 ms) exemplarily in Figure 4b. We further investigated whether the droplet volume varied before and after a trigger signal as shown in the box plot in Figure 4c. This figure shows that the droplet volumes are not significantly different before and after the trigger. Similar findings apply to f_b and f_{b*}.

Further, we investigated how $\Delta\phi$ varied with repetitions of the same stimulus (U_{AC} = 250 V at 100 Hz, $t_{w,AC}$ = 10 ms). Out of 14 consecutive stimuli, the resulting $\Delta\phi$ values ranged from 3 to 90 ms. Since the droplets have a finite reproducible size, this range of phase shift is suitable for phase synchronization between the droplet and the XFEL pulse. Finally, we also investigated if the phase shift induced through triggering in mode 2 can be achieved in droplets containing crystals. We therefore tested mode 2 with lysozyme crystals in the mother liquor (see Supporting Information for details of crystallization conditions). Figure 4d depicts droplets containing lysozyme crystals generated at a base frequency of 10.6 Hz. As shown in Figure 4d, a phase shift is apparent after the triggering event due to a larger droplet distance corresponding to t_s. In summary, mode 2 showed that short AC triggers were able to cause a phase shift in f_b without affecting f_{b*} after the stimulus. We also showed that the size of the droplets remained stable before and after the phase change, and we demonstrated triggering in mode 2 with an aqueous solution containing lysozyme crystals. This mode has the potential for synchronizing droplets that are out of phase but at the same frequency as the pulsed XFELs for SFX experiments.

Mode 3: Tuning the Droplet Frequency. In mode 3, we explored whether an electrical trigger can induce a change in the frequency of a continuous stream of droplets to improve synchronization with an XFEL for the duration of the applied trigger without altering flow rates. Even if flow rate control instrumentation would allow fine-tuning of the droplet generation frequency, any adjustment in flow conditions requires hydrostatic pressure changes, which induce instability in the droplet generation and generate droplets irregularly with a large variation in droplet size.[38] Droplet generation may take up to 30 min to stabilize, depending on the flow conditions, and lost time is always disadvantageous for an XFEL experiment. Thus, increasing the droplet generation frequency (f_t), without changing flow rates and affecting adjacent flow streams, is a useful technique.

To operate the droplet generator in mode 3, a continuous stream of droplets is generated at f_b by holding Q_o and Q_a constant for a range of AC potentials ($100 \leq U_{AC} \leq 400$ V) with a frequency (f_u = 100 Hz) for $t_{w,AC}$ > 100 ms. We characterized the relationship between U_{AC} and f_t at the T-junction using high- (>14 psi) and low-pressure (<14 psi) systems, as demonstrated in Figure 5a. Before the trigger, f_b was 49.1 ± 5.7 Hz and 5.6 ± 0.3 Hz for high- and low-pressure settings, respectively. By increasing U_{AC}, f_b increased to f_t. The increase in f_t as compared with f_b is not very evident between 0 and 240 V, but it becomes more significant after 250 V for both pressure systems with a maximum of an approximately 4-fold increase. Video S3 (Supporting Information) shows acceleration of a droplet frequency under various AC trigger signals in the device.

In addition to this, we also tested the stability of the droplet generation related to f_b and f_{b*}. As shown in Figure 5b, we observed that f_t settled to f_{b*} after the electrical stimulus was stopped, and f_{b*} is similar to f_b within error margins. This demonstrates that the droplet generation frequency only changes during the application of an electrical stimulus and remains unaffected otherwise. We also tested mode 3 for a duration of 5 min and successfully observed the change from f_b to f_t for the entire duration. In summary, mode 3 allows frequency increments in both high- and low-pressure systems, indicating that the increase in droplet generation is independent of the fluidic setup. While the tuning of the droplet frequency was demonstrated with mode 3, the droplet generation frequency becomes unstable if the applied stimulus is above a certain intensity U_{AC} or frequency f_u. We attribute this to electrical instability, which is illustrated in Figure S2.

DOI: 10.1021/acs.analchem.9b01449
Anal. Chem. 2019, 91, 9792−9799

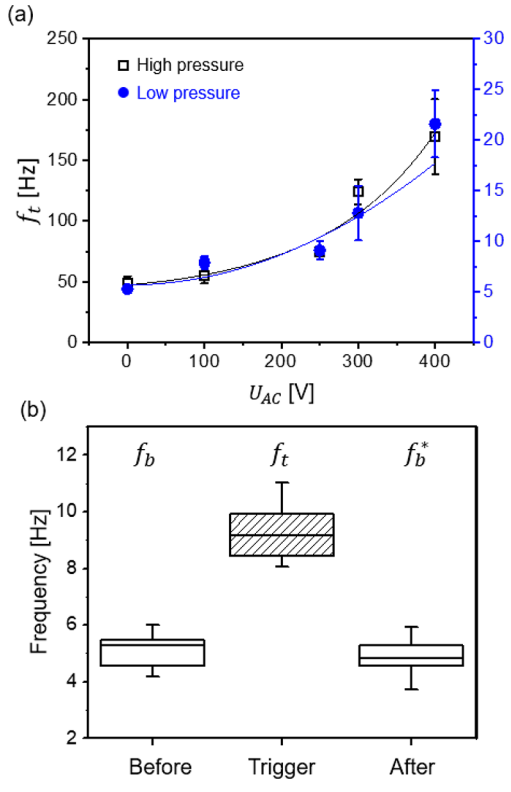

Figure 5. (a) Dependence of the achieved droplet generation frequency (f_t) on the applied AC amplitude (U_{AC}) at f_u = 100 Hz in both high-pressure (black) and low-pressure (blue) systems. The base frequency was 49.1 ± 5.7 Hz and 5.6 ± 0.3 Hz for high and low pressure, respectively. Droplet volumes ranged from 374 ± 8 pL for no potential applied, over 367 ± 8 pL for 100 V, 246 ± 13 pL for 250 V, 139 ± 16 pL for 300 V to 105 ± 13 pL for 400 V. The lines represent quadratic curve fits. Error bars represent the standard deviation. Some error bars in (a) are obscured by the size of the symbol. (b) Analysis of f_b 2 min before and after the trigger signal for U_{AC} = 250 V at f_u = 100 Hz, $t_{w,AC}$ = 1 s. Droplet generation frequencies, f_b, f_t, and f_{b*}, were 5.0 ± 0.4 Hz, 9.2 ± 0.7 Hz, and 4.7 ± 0.5 Hz, respectively. The droplet generation frequency is accelerated during $t_{w,AC}$, and f_{b*} is similar to f_b, within error margins. In the box plots, boxes extend from the 25th to the 75th percentiles with a line at the median. Whiskers extend to the max/min data points.

Above a certain U_{AC} (or f_u) however, the droplet size and frequency becomes unstable, leading to an "electro-spraying" regime, as illustrated in Figure S2. Clearly, in extreme cases, f_b can no longer be increased to a stable f_t during triggering, but rather results in irregularly sized droplets and irregular frequencies. It is also evident that the wetting properties change, as the aqueous droplets contact and wet the microchannel walls.

We note that droplet volumes ranged from 374 ± 8 pL for no potential applied, over 367 ± 8 pL for 100 V, 246 ± 13 pL for 250 V, 139 ± 16 pL for 300 V to 105 ± 13 pL for 400 V. These droplet volumes as well as those for mode 1 and 2 (see above) are comparable in magnitude to the droplets (~80 μm in diameter) obtained through piezoelectric droplet triggering as reported by Mafune et al.[18] Further comparing to piezoelectric droplet generation, we note that the latter cannot be easily interfaced with a mix-and-diffuse serial crystallography setup and that the here reported droplet triggering approach is fully compatible with regular crystal suspension delivery, including sample shaking to prevent crystal settling and cooling to avoid degradation. Our approach thus is favorable to avoid clogging and decreases in crystal hit rates over time as previously reported with piezoelectric droplet generation.[18] We note that similar drawbacks are also to be expected with ADE droplet approaches.

On the basis of the achieved electrically induced triggering, we investigated two major phenomena previously described in literature that could be responsible for the here demonstrated effects,[39] namely, electrowetting on dielectrics (EWOD) and dielectrophoresis (DEP). Electrowetting on dielectrics (EWOD) refers to changes in the contact angle of a dielectric material initiated upon application of a voltage. The control of wettability on a dielectric surface is allowed by controlling the interfacial energy changes between the liquid and the surface.[32] Similarly, in the droplet generator, the interfacial energies of the involved surfaces may be altered, leading to the release of aqueous droplets. The major force (F_w) acting on the aqueous liquid on a dielectric substrate is given as[39,40]

$$F_w = \alpha \frac{U^2}{d_{wall}} \tag{2}$$

where the prefactor, α, is the ratio of involved permittivity and a correction factor $\frac{\varepsilon_0 \varepsilon_d}{2}$.[40,41] Here, ε_0 denotes the permittivity of vacuum and ε_d, the dielectric constant of the insulator (*i.e.*, the photoresist employed to fabricate the 3D printed device), U is the applied voltage, and d_{wall} is the thickness of the dielectric layer. A larger F_w is thus induced through larger applied potentials and a shorter d_{wall}. This was observed in our study, as lower threshold voltage amplitudes were required for decreased d_{wall} as observed in mode 1 (Figure 3e). Moreover, the study conducted in mode 3 showed that increased voltage amplitudes lead to acceleration of the droplet frequency. This can also be explained with increased F_w as demonstrated in Figure 5a,b. In addition, analysis of the video sequences demonstrated wetting of the hydrophobic inner channel walls with the aqueous droplets, when being released from the T-junction upon triggering. This effect is dependent on employed flow rates, droplet sizes, and applied voltage amplitudes, but is a strong indication for EWOD effects during electrical triggering. Similar arguments may be used for the effect of DEP on droplet release, as the dielectrophoretic force scales with the applied potential squared.[42,43] In DEP, a polarizable particle or a polarizable interface experiences an attractive or repulsive force under a nonuniform electric field.[39,44] In our case, the electrode geometry used in the droplet generator induces a nonuniform electric field. While the detailed mechanism of DEP at the T-junction needs further study, it seems reasonable that DEP forces may push the aqueous−oil interface into the T-junction thereby facilitating droplet release. However, previous reports have shown that DEP forces are typically weaker than EWOD effects in the frequency regime studied here.[30,37] Therefore, it seems likely that electrowetting forces dominate the droplet release in the presented device. A more detailed study, however, needs to be conducted to quantitatively compare the magnitude of EWOD and DEP forces.

CONCLUSIONS

We demonstrated a 3D printed microfluidic platform with embedded gallium electrodes to enhance control of aqueous droplet generation in a stream of oil. The microfluidic T-junction with embedded gallium electrodes can be operated in

DOI: 10.1021/acs.analchem.9b01449
Anal. Chem. 2019, 91, 9792−9799

three different modes to generate droplets. First, on-demand droplets can be generated through programmable DC potentials. We demonstrated on-demand droplet generation with a maximum frequency of 1.7 Hz. Future optimization and device design may likely allow an increase in the on-demand droplet generation frequency to match current XFEL repetition rates. Second, the phase of the droplet generation frequency can be tuned under short AC signals that can be employed to assist the synchronization of the aqueous droplets with the XFEL pulses. Third, the droplet generation frequency can be increased by AC trigger signals without hampering droplet generation stability, before and after the trigger. In addition, we discuss the origin of the observed phenomena and conclude that electrowetting is predominantly responsible for the observed droplet triggering effects. This innovative approach of controlling droplet production and delivery in the path of X-rays can be utilized to improve synchronization of droplets and the X-ray beam and consequently play a crucial role in saving protein crystal sample in SFX experiments. In addition, 3D printing technology will allow for future integration of the 3D printed droplet generator with 3D printed GDVN injectors recently developed for XFEL sample delivery.

■ ASSOCIATED CONTENT

Supporting Information

The Supporting Information is available free of charge on the ACS Publications website at DOI: 10.1021/acs.analchem.9b01449.

Materials and chemicals, droplet observation and data analysis, supplementary figure and table (PDF)

Droplet on-demand generation events using a DC trigger signal, mode 1 (AVI)

Demonstration of phases shift, mode 2 (AVI)

Acceleration of droplets under the various AC trigger signal, mode 3 (MOV)

■ AUTHOR INFORMATION

Corresponding Author

*E-mail: Alexandra.Ros@asu.edu. Phone: +1-480-965-5323. Fax: +1-480-965-7954.

ORCID

Alexandra Ros: 0000-0001-7709-8331

Notes

The authors declare no competing financial interest.

■ ACKNOWLEDGMENTS

We thank Dr. Richard Kirian and Dr. Uwe Weierstall from the Department of Physics at Arizona State University for the use of the high-speed camera. This work was supported by the STC Program of the National Science Foundation (NSF) through BioXFEL under Agreement No. 1231306 and the National Institutes of Health Award No. R01GM095583. We thank Dr. Seo in the School of Molecular Sciences at Arizona State University for providing access to the viscometer.

■ REFERENCES

(1) Spence, J. C. H. *IUCrJ* **2017**, *4*, 322−339.

(2) Boutet, S.; Lomb, L.; Williams, G. J.; Barends, T. R. M.; Aquila, A.; Doak, R. B.; Weierstall, U.; DePonte, D. P.; Steinbrener, J.; Shoeman, R. L.; Messerschmidt, M.; Barty, A.; White, T. A.; Kassemeyer, S.; Kirian, R. A.; Seibert, M. M.; Montanez, P. A.; Kenney, C.; Herbst, R.; Hart, P.; et al. *Science* **2012**, *337*, 362−364.

(3) Liu, W.; Wacker, D.; Gati, C.; Han, G. W.; James, D.; Wang, D.; Nelson, G.; Weierstall, U.; Katritch, V.; Barty, A.; Zatsepin, N. A.; Li, D.; Messerschmidt, M.; Boutet, S.; Williams, G. J.; Koglin, J. E.; Seibert, M. M.; Wang, C.; Shah, S. T. A.; Basu, S.; et al. *Science* **2013**, *342*, 1521−1524.

(4) Kupitz, C.; Basu, S.; Grotjohann, I.; Fromme, R.; Zatsepin, N. A.; Rendek, K. N.; Hunter, M. S.; Shoeman, R. L.; White, T. A.; Wang, D.; James, D.; Yang, J.-H.; Cobb, D. E.; Reeder, B.; Sierra, R. G.; Liu, H.; Barty, A.; Aquila, A. L.; Deponte, D.; Kirian, R. A.; et al. *Nature* **2014**, *513*, 261.

(5) Martin-Garcia, J. M.; Conrad, C. E.; Coe, J.; Roy-Chowdhury, S.; Fromme, P. *Arch. Biochem. Biophys.* **2016**, *602*, 32−47.

(6) Frank, M.; Carlson, D. B.; Hunter, M. S.; Williams, G. J.; Messerschmidt, M.; Zatsepin, N. A.; Barty, A.; Benner, W. H.; Chu, K.; Graf, A. T.; Hau-Riege, S. P.; Kirian, R. A.; Padeste, C.; Pardini, T.; Pedrini, B.; Segelke, B.; Seibert, M. M.; Spence, J. C. H.; Tsai, C.-J.; Lane, S. M.; et al. *IUCrJ* **2014**, *1*, 95−100.

(7) Chapman, H. N.; Fromme, P.; Barty, A.; White, T. A.; Kirian, R. A.; Aquila, A.; Hunter, M. S.; Schulz, J.; DePonte, D. P.; Weierstall, U.; Doak, R. B.; Maia, F. R. N. C.; Martin, A. V.; Schlichting, I.; Lomb, L.; Coppola, N.; Shoeman, R. L.; Epp, S. W.; Hartmann, R.; Rolles, D.; et al. *Nature* **2011**, *470*, 73−77.

(8) Johansson, L. C.; Stauch, B.; Ishchenko, A.; Cherezov, V. *Trends Biochem. Sci.* **2017**, *42*, 749−762.

(9) Conrad, C. E.; Basu, S.; James, D.; Wang, D.; Schaffer, A.; Roy-Chowdhury, S.; Zatsepin, N. A.; Aquila, A.; Coe, J.; Gati, C.; Hunter, M. S.; Koglin, J. E.; Kupitz, C.; Nelson, G.; Subramanian, G.; White, T. A.; Zhao, Y.; Zook, J.; Boutet, S.; Cherezov, V.; et al. *IUCrJ* **2015**, *2*, 421−430.

(10) Boutet, S., Fromme, Petra, Hunter, Mark S. *X-ray Free Electron Lasers*; Springer International Publishing: Switzerland, 2018.

(11) Weierstall, U.; James, D.; Wang, C.; White, T. A.; Wang, D.; Liu, W.; Spence, J. C. H.; Bruce Doak, R.; Nelson, G.; Fromme, P.; Fromme, R.; Grotjohann, I.; Kupitz, C.; Zatsepin, N. A.; Liu, H.; Basu, S.; Wacker, D.; Won Han, G.; Katritch, V.; Boutet, S.; et al. *Nat. Commun.* **2014**, *5*, 3309.

(12) Sierra, R. G.; Weierstall, U.; Oberthuer, D.; Sugahara, M.; Nango, E.; Iwata, S.; Meents, A. In *X-ray Free Electron Lasers: A Revolution in Structural Biology*; Boutet, S., Fromme, P., Hunter, M. S., Eds.; Springer International Publishing: Cham, 2018; pp 109−184.

(13) Liu, W.; Wacker, D.; Wang, C.; Abola, E.; Cherezov, V. *Philos. Trans. R. Soc., B* **2014**, *369*, 20130314.

(14) Wiedorn, M. O.; Oberthür, D.; Bean, R.; Schubert, R.; Werner, N.; Abbey, B.; Aepfelbacher, M.; Adriano, L.; Allahgholi, A.; Al-Qudami, N.; Andreasson, J.; Aplin, S.; Awel, S.; Ayyer, K.; Bajt, S.; Barák, I.; Bari, S.; Bielecki, J.; Botha, S.; Boukhelef, D.; et al. *Nat. Commun.* **2018**, *9*, 4025.

(15) Altarelli, M.; Mancuso, A. P. *Philos. Trans. R. Soc. London, B, Biol. Sci.* **2014**, *369*, 20130311.

(16) Sierra, R. G.; Laksmono, H.; Kern, J.; Tran, R.; Hattne, J.; Alonso-Mori, R.; Lassalle-Kaiser, B.; Glockner, C.; Hellmich, J.; Schafer, D. W.; Echols, N.; Gildea, R. J.; Grosse-Kunstleve, R. W.; Sellberg, J.; McQueen, T. A.; Fry, A. R.; Messerschmidt, M. M.; Miahnahri, A.; Seibert, M. M.; Hampton, C. Y.; et al. *Acta Crystallogr., Sect. D: Biol. Crystallogr.* **2012**, *68*, 1584−1587.

(17) Sierra, R. G.; Gati, C.; Laksmono, H.; Dao, E. H.; Gul, S.; Fuller, F.; Kern, J.; Chatterjee, R.; Ibrahim, M.; Brewster, A. S.; Young, I. D.; Michels-Clark, T.; Aquila, A.; Liang, M.; Hunter, M. S.; Koglin, J. E.; Boutet, S.; Junco, E. A.; Hayes, B.; Bogan, M. J.; et al. *Nat. Methods* **2016**, *13*, 59.

(18) Mafune, F.; Miyajima, K.; Tono, K.; Takeda, Y.; Kohno, J.-y.; Miyauchi, N.; Kobayashi, J.; Joti, Y.; Nango, E.; Iwata, S.; Yabashi, M. *Acta Cryst. D* **2016**, *72*, 520−523.

(19) Tono, K. *High Power Laser Sci. Eng.* **2017**, *5*, e7.

(20) Kubo, M.; Nango, E.; Tono, K.; Kimura, T.; Owada, S.; Song, C.; Mafune, F.; Miyajima, K.; Takeda, Y.; Kohno, J.-y.; Miyauchi, N.; Nakane, T.; Tanaka, T.; Nomura, T.; Davidsson, J.; Tanaka, R.;

DOI: 10.1021/acs.analchem.9b01449
Anal. Chem. 2019, 91, 9792−9799

Murata, M.; Kameshima, T.; Hatsui, T.; Joti, Y.; et al. *J. Synchrotron Radiat.* **2017**, *24*, 1086−1091.
(21) Roessler, C. G.; Agarwal, R.; Allaire, M.; Alonso-Mori, R.; Andi, B.; Bachega, J. F. R.; Bommer, M.; Brewster, A. S.; Browne, M. C.; Chatterjee, R.; Cho, E.; Cohen, A. E.; Cowan, M.; Datwani, S.; Davidson, V. L.; Defever, J.; Eaton, B.; Ellson, R.; Feng, Y.; Ghislain, Lucien P.; et al. *Structure* **2016**, *24*, 631−640.
(22) Fuller, F. D.; Gul, S.; Chatterjee, R.; Burgie, E. S.; Young, I. D.; Lebrette, H.; Srinivas, V.; Brewster, A. S.; Michels-Clark, T.; Clinger, J. A.; Andi, B.; Ibrahim, M.; Pastor, E.; de Lichtenberg, C.; Hussein, R.; Pollock, C. J.; Zhang, M.; Stan, C. A.; Kroll, T.; Fransson, T.; et al. *Nat. Methods* **2017**, *14*, 443.
(23) Grünbein, M. L.; Nass Kovacs, G. *Acta Cryst. D* **2019**, *75*, 178.
(24) Beyerlein, K. R.; Dierksmeyer, D.; Mariani, V.; Kuhn, M.; Sarrou, I.; Ottaviano, A.; Awel, S.; Knoska, J.; Fuglerud, S.; Jonsson, O.; Stern, S.; Wiedorn, M. O.; Yefanov, O.; Adriano, L.; Bean, R.; Burkhardt, A.; Fischer, P.; Heymann, M.; Horke, D. A.; Jungnickel, K. E. J.; et al. *IUCrJ* **2017**, *4*, 769−777.
(25) Echelmeier, A.; Nelson, G.; Abdallah, B. G.; James, D.; Roy-Chowdhury, S.; Tolstikova, A.; Mariani, V.; Kirian, R. A.; Oberthüer, D.; Dörner, K.; Fromme, P.; Chapman, H. N.; Weierstall, U.; Spence, J. C. H.; Ros, A. Biphasic droplet-based sample delivery of protein crystals for serial femtosecond crystallography with an X-ray free electron laser*MicroTAS 2015 - 19th International Conference on Miniaturized Systems for Chemistry and Life Sciences*, Gyeongju, South Korea, October 25−29, 2015; pp 1374−1376
(26) Chen, J.-S.; Jiang, J.-H. *Chin. J. Anal. Chem.* **2012**, *40*, 1293−1300.
(27) Gu, H.; Duits, M. H. G.; Mugele, F. *Int. J. Mol. Sci.* **2011**, *12*, 2572−2597.
(28) Baroud, C. N.; Gallaire, F.; Dangla, R. *Lab Chip* **2010**, *10*, 2032−2045.
(29) Pit, A. M.; Duits, M. H. G.; Mugele, F. *Micromachines* **2015**, *6*, 1768−1793.
(30) Zhu, P.; Wang, L. *Lab Chip* **2017**, *17*, 34−75.
(31) Echelmeier, A.; Cruz Villarreal, J.; Kim, D.; Gandhi, S.; Egatz-Gomez, A.; Quintana, S.; Coe, J.; Brehm, G.; Messerschmidt, M.; Meza-Aguilar, J. D.; Weinhaussen, B.; Mills, G.; Vagovic, P.; Kim, Y.; Schultz, J.; Döner, K.; Mancuso, A.; Weierstall, U.; Spence, J. C. H.; Chapman, H. N., et al. Segmented Flow Generator for Serial Crystallography at X-Ray Free Electron Lasers. Manuscript in preparation.
(32) Mugele, F.; Baret, J. C. *J. Phys.: Condens. Matter* **2005**, *17*, R705−R774.
(33) Mugele, F.; Duits, M.; van den Ende, D. *Adv. Colloid Interface Sci.* **2010**, *161*, 115−123.
(34) Pollack, M. G.; Shenderov, A. D.; Fair, R. B. *Lab Chip* **2002**, *2*, 96−101.
(35) Echelmeier, A.; Kim, D.; Cruz Villarreal, J.; Coe, J.; Quintana, S.; Brehm, G.; Egatz-Gomez, A.; Sierra, R.; Zatsepin, N.; Kirian, R.; Grant, T. D.; Fromme, P.; Ros, A. *J. Appl. Crystallogr.* **2019**, in review.
(36) Lin, Y.; Gordon, O.; Khan, M. R.; Vasquez, N.; Genzer, J.; Dickey, M. D. *Lab Chip* **2017**, *17*, 3043−3050.
(37) Coe, J. *Life In Motion: Visualizing Biomacromolecules By Time-Resolved Serial Femtosecond Crystallography*. Ph.D. Thesis, Arizona State University, 2018.
(38) Chong, Z. Z.; Tan, S. H.; Gañán-Calvo, A. M.; Tor, S. B.; Loh, N. H.; Nguyen, N. T. *Lab Chip* **2016**, *16*, 35−58.
(39) Jones, T. B. *Langmuir* **2002**, *18*, 4437−4443.
(40) Kang, K. H. *Langmuir* **2002**, *18*, 10318−10322.
(41) Jones, T. B. *Mech. Res. Commun.* **2009**, *36*, 2−9.
(42) Jones, T. B. *Electromechanics of Particles*; Cambridge University Press: New York, 1995; p 265.
(43) Pohl, H. A. *Dielectrophoresis: the behavior of neutral matter in nonuniform electric fields*; Cambridge University Press: New York, 1978.
(44) Kim, D.; Sonker, M.; Ros, A. *Anal. Chem.* **2019**, *91*, 277−295.

DOI: 10.1021/acs.analchem.9b01449
Anal. Chem. 2019, 91, 9792−9799